

Cross-Modal Alignment and Fusion for RGB-D Transmission-Line Defect Detection*

Jiaming Cui^a, Wenqiang Li^b, Shuai Zhou^{b,c}, Ruifeng Qin^b, Feng Shen^{b,*}

^a*School of Mechatronics Engineering, Harbin Institute of Technology, Harbin, 150001, China*

^b*School of Instrument Science and Engineering, Harbin Institute of Technology, Harbin, 150001, China*

^c*Electric Power Research Institute, Yunnan Power Grid Co., Ltd., Kunming, 650217, China*

Abstract

Transmission line defect detection presents persistent challenges for automated inspection systems due to the prevalence of small-scale defects, complex backgrounds, and varying illumination conditions in UAV-captured imagery. While existing deep learning methods have achieved considerable progress using RGB images alone, they remain fundamentally limited in distinguishing geometrically subtle defects from visually similar background elements, particularly when chromatic contrast is insufficient. This paper proposes CMAFNet, a Cross-Modal Alignment and Fusion Network that integrates RGB appearance and depth geometry through a principled “purify-then-fuse” paradigm for robust defect detection. The architecture comprises two complementary mechanisms: a Semantic Recomposition Module that performs dictionary-based feature purification by projecting representations into a learned codebook with controllable capacity, thereby filtering modality-specific noise while preserving defect-relevant patterns; and a Contextual Semantic Integration Framework that establishes global spatial dependencies through partial-channel attention, enabling the network to leverage structural priors for semantic disambiguation. Position-wise normalization within the purification stage transforms cross-modal alignment from implicit weight-based learning into explicit reconstruction-driven enhancement, ensuring that heterogeneous RGB and depth features attain compatible statistical distributions prior to fusion. Extensive experiments on TL-RGBD, a large-scale benchmark where 94.5% of annotated instances qualify as small objects, demonstrate that CMAFNet achieves 32.2% mAP₅₀ and 12.5% AP_s, surpassing the best baseline by 9.8 and 4.0 absolute percentage points, respectively. The lightweight configuration attains 24.8% mAP₅₀ at 228 FPS with only 4.9M parameters, outperforming all YOLO variants while matching larger transformer-based detectors at a fraction of their computational cost.

Keywords: Defect detection, RGB-D fusion, Cross-modal alignment, Small object detection, Transmission line inspection

1. Introduction

Electrical power transmission networks constitute the critical infrastructure of modern society, serving as the backbone for energy delivery across industrial, commercial, and residential sectors (Zhang et al., 2024b; Luo et al., 2023). Transmission lines, as the most exposed and geographically dispersed components of power grids, are continuously subjected to harsh environmental conditions, mechanical stress, and material degradation over extended operational periods (Shen et al., 2025; Deng et al., 2024). Common defects including insulator contamination, conductor corrosion, fitting damage, and bird nest interference pose substantial risks to grid reliability and public safety if left undetected (Bao et al., 2022; Zhang et al., 2025a; Cheng and Liu, 2024). The timely and accurate identification of such defects is therefore essential not only for preventing catastrophic

failures and large-scale blackouts but also for optimizing maintenance scheduling and extending asset lifespan (Yang et al., 2023). Given the vast scale of transmission networks and the increasing demand for grid resilience, automated and intelligent defect detection has emerged as a pressing research priority in both the power engineering and computer vision communities (Li et al., 2023; Zhang et al., 2025b).

Conventional approaches to transmission line defect detection have long confronted significant challenges in achieving reliable and scalable performance (Liu et al., 2020; Song et al., 2014). Manual inspection, which dominated early practices, typically relies on human operators either physically traversing transmission corridors or remotely controlling inspection platforms along predefined pathsa process that is inherently hazardous to crew safety, operationally inefficient, and cost-prohibitive for large-scale grid networks (Pouliot and Montambault, 2012; Xu et al., 2022a). These practical constraints have driven the power industry toward automated inspection systems to ensure operational stability and safety, with intelligent visual inspection emerging as a particularly promising paradigm that enables efficient defect identification while substantially reducing manual annotation burdens and field deployment risks (Wang et al., 2025; Yi et al., 2025).

The rapid proliferation of unmanned aerial vehicles equipped

*This work was supported by the National Natural Science Foundation of China under Grant 52371351, Grant 61673128, Grant 61573117, and Grant 41627801.

*Corresponding author.

Email addresses: hitcjm@stu.hit.edu.cn (Jiaming Cui), wengli@stu.hit.edu.cn (Wenqiang Li), 22B901046@stu.hit.edu.cn (Shuai Zhou), qrf_951208@126.com (Ruifeng Qin), fshen@hit.edu.cn (Feng Shen)

with high-resolution RGB cameras has substantially transformed data acquisition paradigms, enabling efficient large-scale image collection across extensive transmission corridors (Xu et al., 2022b; da Silva et al., 2020). Building upon this advancement, numerous deep learning-based detection frameworks have been proposed, predominantly leveraging convolutional neural networks such as YOLO variants with attention mechanisms for enhanced feature extraction (Wang et al., 2024), Faster R-CNN with aerial image augmentation strategies (Cao et al., 2023), and lightweight architectures incorporating multiscale feature fusion for small defect detection (Ma et al., 2025; Wu et al., 2025). Self-supervised learning methods utilizing vision transformers have further been explored to address the challenge of limited labeled defect samples in practical inspection scenarios (Zhang et al., 2024a). Despite these methodological advances, RGB-based approaches remain fundamentally constrained by their reliance on single-modal visual information, struggling with defects exhibiting low chromatic contrast against cluttered backgrounds, geometrically ambiguous damage patterns, and frequent occlusions caused by vegetation or atmospheric interference (He et al., 2025; Chen et al., 2025). A critical trade-off persists between detection accuracy and computational efficiency: high-precision models typically demand substantial computational resources measured in tens of GFLOPs, rendering them impractical for real-time deployment on resource-constrained UAV platforms, whereas lightweight alternatives often sacrifice detection performance to achieve acceptable inference speeds (Tan et al., 2020; Chen et al., 2024). Fundamentally, RGB imagery alone cannot reliably capture critical depth-related characteristics including surface deformation, structural protrusion, and spatial displacement that are essential for distinguishing subtle defects from benign surface variations under complex environmental conditions (Li et al., 2025; Gupta et al., 2014).

The inherent limitations of single-modal approaches have motivated the exploration of multi-modal fusion strategies that integrate RGB appearance with depth geometry to achieve more robust defect detection. According to a recent comprehensive survey on deep multi-modal data fusion (Zhao et al., 2024), existing fusion paradigms can be broadly categorized into raw-data-level fusion, hierarchical feature fusion, and decision-level fusion. Raw-data-level fusion concatenates RGB and depth channels along the input dimension before feeding them into a single encoder, which maximally preserves original information from each modality while minimizing computational cost through a unified backbone (Zhao et al., 2024). However, this approach forces the network to learn cross-modal correspondences implicitly from the earliest layers, which proves suboptimal when RGB and depth modalities exhibit fundamentally different statistical properties and semantic structures. At the opposite extreme, decision-level fusion delays cross-modal interaction until the final prediction stage, offering straightforward implementation but providing limited interpretability of multi-modal interactions and suffering from vulnerability to single-modality failures (Zhao et al., 2024). Between these two paradigms, hierarchical feature fusion has emerged as a principled framework that leverages the multi-level representations

extracted from deep networks to establish cross-modal correspondences at varying levels of abstraction. By employing dedicated encoder branches for each modality and progressively aggregating their features at multiple pyramid levels, hierarchical fusion offers two key advantages: the flexibility to determine where and how many hierarchical features are fused for specific tasks, and the natural compatibility with attention mechanisms that can upgrade the connections between multi-modal features at corresponding levels (Zhao et al., 2024). Nevertheless, existing hierarchical fusion methods predominantly adopt static fusion strategies such as fixed element-wise summation or simple concatenation followed by convolution that lack adaptability to the dynamic variations inherent in transmission line inspection scenarios. When RGB features suffer from illumination artifacts or depth features contain boundary discontinuities and quantization noise, static fusion propagates these modality-specific corruptions into the shared representation, ultimately degrading rather than enhancing detection performance.

To address the foregoing limitations, this paper proposes CMAFNet, a Cross-Modal Alignment and Fusion Network that integrates RGB appearance and depth geometry through a “purify-then-fuse” paradigm for transmission line defect detection. The proposed architecture proceeds in three stages: intra-modal semantic purification that suppresses noise and stabilizes feature distributions within each modality branch, cross-modal fusion with explicit semantic enhancement that constructs shared representations emphasizing common discriminative patterns while attenuating modality-private residuals, and refined semantic guidance that propagates high-quality shared semantics reliably to small-object-sensitive detection layers. This three-stage design embodies a core principle: cross-modal fusion should not operate directly on raw backbone features containing substantial modality-specific noise; instead, each modality stream must first undergo semantic purification to create favorable conditions for subsequent alignment. Two novel modules—the Semantic Dictionary Injection Refiner and the Global Semantic Refinement Framework—are strategically deployed throughout the network to realize this paradigm. Extensive experiments on TL-RGBD, a large-scale benchmark where 94.5% of annotated instances are small objects, demonstrate that CMAFNet achieves state-of-the-art performance across multiple evaluation criteria while maintaining competitive inference efficiency suitable for practical deployment.

The main contributions of this paper are summarized as follows:

1. We propose CMAFNet, a Cross-Modal Alignment and Fusion Network that addresses RGB-D transmission-line defect detection through a principled “purify-then-fuse” paradigm. Unlike conventional fusion strategies that operate directly on noisy backbone features, this architecture first suppresses modality-specific artifacts within each branch before constructing cross-modal representations, thereby establishing favorable statistical conditions for subsequent alignment. Extensive experiments

on a challenging benchmark dominated by small objects demonstrate that CMAFNet achieves state-of-the-art performance across multiple evaluation metrics while maintaining competitive inference efficiency.

2. We introduce the Semantic Recomposition Module, a dictionary-based feature purification mechanism that projects representations into a learned codebook with controllable capacity. By creating an information bottleneck through structured retrieval and residual injection, SRM filters modality-specific noise—including illumination artifacts in RGB imagery and quantization errors in depth maps—while preserving discriminative patterns essential for defect recognition. The position-wise normalization embedded within SRM transforms cross-modal alignment from implicit weight-based learning into explicit reconstruction-driven enhancement, ensuring that heterogeneous RGB and depth features attain compatible statistical distributions prior to fusion.
3. We design the Contextual Semantic Integration Framework, a global attention mechanism that captures long-range dependencies through partial-channel multi-head self-attention. CSIF addresses the limitation that purely convolutional fusion operates within bounded receptive fields and consequently fails to exploit structural priors—such as the regular arrangement of insulator strings and spatial relationships among transmission components—for semantic disambiguation. The partial-channel design, combined with the Adaptive Semantic Regulation Mechanism, prevents the detail erosion that typically accompanies full-channel global attention, thereby preserving the fine-grained discrimination essential for small-object detection.

The remainder of this paper is organized as follows. Section 2 elaborates the proposed CMAFNet architecture, detailing the dual-branch backbone, hierarchical fusion strategy, and the design principles underlying SRM and CSIF. Section 3 describes the experimental setup, presents quantitative comparisons with state-of-the-art methods, and provides ablation analyses that validate the contribution of each architectural component. Section 4 concludes the paper with a discussion of limitations and directions for future research.

2. Method

2.1. Overview of Network Architecture

The proposed Cross-Modal Alignment and Fusion Network addresses the fundamental challenges inherent in RGB-D transmission-line defect detection, where targets of interest are predominantly small and exhibit subtle visual signatures across heterogeneous modality representations. Our architecture departs from conventional single-stream detectors by introducing a dual-branch encoding paradigm coupled with progressive cross-modal fusion, thereby enabling the network to preserve modality-specific discriminative features while constructing semantically aligned multimodal representations. The overall architecture comprises three principal components: a dual par-

allel backbone for independent modality encoding, hierarchical fusion layers for cross-modal feature integration, and a Feature Pyramid Network augmented with Path Aggregation Network for multi-scale detection. Two specialized modules—the Semantic Recomposition Module and the Contextual Semantic Integration Framework—are strategically embedded throughout the network to address the critical issues of intra-modal feature purification and cross-modal semantic enhancement, respectively. Fig. 1 illustrates the complete network topology and the information flow across all architectural components.

2.1.1. Backbone: Dual Parallel Branches

The backbone architecture employs a symmetric dual-branch design that processes RGB imagery and depth maps through independent encoding pathways. This parallel configuration is motivated by the observation that RGB and depth modalities encode fundamentally distinct visual properties: RGB channels capture texture, color gradients, and photometric variations, whereas depth maps provide geometric structure, spatial discontinuities, and distance-based saliency. Forcing these heterogeneous signals through a shared encoder would inevitably compromise the integrity of modality-specific representations, as the network would be compelled to learn entangled features that inadequately capture the unique discriminative characteristics of each input stream.

Each branch follows an identical structural template while maintaining entirely separate learnable parameters, thereby ensuring that modality-specific feature distributions are preserved throughout the encoding process. The encoding pathway begins with an initial convolutional layer that operates at stride 2, reducing the spatial resolution to P_1 scale while projecting raw inputs into a 64-dimensional feature space. Subsequent stages progressively downsample the feature maps through strided convolutions while expanding channel dimensionality, with P_2 , P_3 , P_4 , and P_5 scales corresponding to spatial reductions of 4 \times , 8 \times , 16 \times , and 32 \times relative to input resolution, respectively. Feature extraction at each scale is accomplished through C3k2 blocks, which implement an efficient variant of the Cross-Stage Partial architecture with kernel-size parameterization, enabling flexible receptive field configuration while maintaining computational efficiency.

The design rationale for maintaining parallel branches rather than early fusion stems from the distinct noise characteristics and information density profiles of the two modalities. Depth measurements from structured-light or time-of-flight sensors exhibit modality-specific artifacts including edge bleeding, missing values at specular surfaces, and quantization noise at extended rangesphenomena that bear no correspondence to the noise distributions present in RGB imagery. By preserving independent encoding pathways through the P_5 scale, the network permits each branch to develop specialized denoising and feature extraction strategies tailored to its respective input modality.

At the P_3 and P_4 scales within each branch, Semantic Recomposition Modules are inserted immediately following the C3k2 feature extraction blocks. These modules serve a critical preparatory function for subsequent cross-modal fusion by

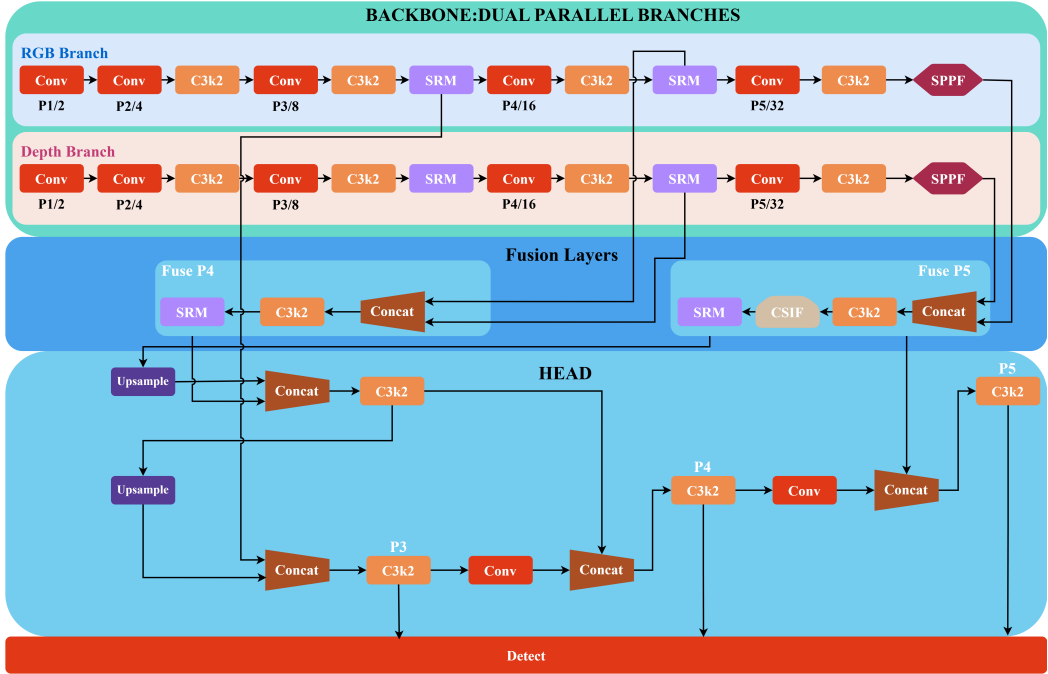


Figure 1: Overall architecture of the proposed Cross-Modal Alignment and Fusion Network. The dual-branch encoder independently processes RGB and depth modalities through symmetric pathways, with Semantic Recomposition Modules deployed at P_3 and P_4 scales for intra-modal semantic purification and cross-modal distribution alignment. Cross-modal fusion is performed at P_4 and P_5 levels, where the Contextual Semantic Integration Framework provides global attention-based context modeling at the deepest semantic scale. The detection head implements bidirectional feature propagation through FPN and PAN pathways for multi-scale defect detection.

projecting branch-specific features into a normalized dictionary space where semantic concepts can be explicitly disentangled and refined. The placement at intermediate scales rather than solely at the deepest layer reflects the particular requirements of small object detection: P_3 and P_4 features retain sufficient spatial resolution to preserve fine-grained structural details essential for localizing compact defects, while possessing adequate semantic abstraction to support meaningful cross-modal correspondence. The branch-level SRM instances employ a compact dictionary configuration of 128 atoms, as the objective at this stage is intra-modal feature refinement rather than comprehensive cross-modal semantic modeling.

The terminal layer of each branch consists of a Spatial Pyramid-Pooling-Fast module applied at the P_5 scale, which aggregates multi-scale contextual information through parallel max-pooling operations with kernel size 5. This configuration expands the effective receptive field without introducing additional downsampling, thereby enriching the semantic content of the deepest features while preserving the spatial correspondence necessary for accurate localization in subsequent detection stages.

2.1.2. Fusion Layers

The fusion architecture implements a hierarchical integration strategy that combines RGB and depth features at the P_4 and P_5 scales, where semantic abstraction is sufficiently mature to support meaningful cross-modal alignment while retaining adequate spatial granularity for precise defect localization. The decision to exclude P_3 from direct fusion and instead

route it exclusively through the RGB pathway to the detection head reflects an empirical observation that shallow-scale features benefit more from modality-specific spatial detail preservation than from premature cross-modal mixing, which can introduce alignment noise that degrades small object detection performance.

At the P_4 fusion point, the network concatenates the SRM-processed features from both branches along the channel dimension, yielding a combined representation of doubled channel depth. This concatenated tensor is subsequently refined through a C3k2 block that learns to extract cross-modal complementary patterns for instance, associating RGB texture signatures of corrosion or mechanical damage with corresponding depth discontinuities indicative of surface deformation. The C3k2 architecture is particularly suited to this fusion stage, as its cross-stage partial connectivity enables efficient gradient flow while the dual-path internal structure can implicitly develop specialized processing for RGB-derived and depth-derived feature subsets within the concatenated input.

Following initial C3k2 refinement, a second Semantic Recomposition Module is applied to the fused P_4 representation. Unlike the branch-level SRM instances that operate with 128-atom dictionaries for intra-modal purification, this fusion-stage module employs an expanded 256-atom dictionary to accommodate the richer semantic vocabulary required for modeling cross-modal correspondences. The dictionary learning mechanism enables explicit encoding of joint RGB-D semantic concepts that cannot be adequately represented within either individual modality such as the characteristic combination of dis-

coloration patterns in RGB imagery with geometric protrusions in depth maps that jointly indicate bird nest accumulation on transmission infrastructure.

The P_5 fusion pathway follows an analogous concatenation-refinement pattern, with the notable addition of a Contextual Semantic Integration Framework inserted between the C3k2 block and the terminal SRM. This module augments the fusion process with attention-based global context modeling, addressing the limitation that purely convolutional fusion operates within bounded receptive fields and may consequently fail to capture long-range dependencies essential for understanding defect patterns that span extended spatial regions. The attention mechanism computes pairwise affinities across spatial positions, enabling features at any location to directly aggregate information from semantically related positions throughout the feature map. This capability proves particularly valuable for transmission-line defect detection, where contextual relationships between components such as the spatial configuration of insulators relative to conductors provide critical diagnostic cues.

The progressive fusion strategy, wherein P_4 features are fused prior to P_5 and both fusion outputs are subsequently connected through the detection head’s feature pyramid, establishes information flow paths that enable deep-layer semantic guidance to inform shallow-layer feature refinement during back-propagation. This design ensures that the learning objective for small object detection at high-resolution scales can influence the cross-modal alignment learned at deeper fusion stages, thereby producing fused representations that are explicitly optimized for the downstream detection task rather than generic feature similarity.

2.1.3. Head

The detection head implements a bidirectional feature pyramid architecture that combines top-down Feature Pyramid Network pathways with bottom-up Path Aggregation Network connections, establishing comprehensive multi-scale feature communication essential for detecting transmission-line defects that manifest across a wide range of spatial extents. This architectural choice is motivated by the observation that transmission infrastructure inspection datasets exhibit extreme scale variation: defects range from millimeter-scale crack initiations visible only at high resolution to meter-scale structural deformations that require broad contextual understanding.

The FPN pathway initiates from the SRM-processed fused P_5 features, which are upsampled by factor 2 through nearest-neighbor interpolation and concatenated with the fused P_4 representation. A C3k2 block refines this combined tensor, learning to propagate high-level semantic information to the intermediate scale while integrating the finer spatial details preserved at P_4 resolution. This refined intermediate representation undergoes further upsampling and concatenation with the RGB branch’s P_3 features, producing the highest-resolution detection features at $P_3/8$ scale. The asymmetric design wherein P_3 receives input solely from the RGB branch rather than from a fused source reflects the observation that depth map resolution limitations and sensor noise characteristics render depth features less reliable at shallow scales, where RGB texture infor-

mation provides superior discriminative power for small defect detection.

The subsequent PAN pathway reverses the information flow direction, propagating fine-grained spatial details from P_3 back toward deeper scales through strided convolutions and feature concatenation. This bottom-up augmentation addresses a fundamental limitation of purely top-down feature pyramids: while FPN effectively distributes semantic information to shallow layers, it cannot propagate the precise localization cues present at high resolution back to deeper layers that may benefit from such spatial detail during classification and regression. The PAN connections ensure that the P_4 and P_5 detection features receive both the semantic richness derived from deep fusion stages and the spatial precision necessary for accurate bounding box regression.

Each scale within the bidirectional pyramid terminates in a detection head that performs classification and localization for objects within a designated size range, with anchor-free prediction formulations that directly regress center coordinates, width, and height. The multi-head configuration enables scale-appropriate feature utilization: $P_3/8$ features detect small defects such as surface cracks and minor hardware damage, $P_4/16$ features handle medium-scale anomalies including insulator contamination and moderate structural displacement, while $P_5/32$ features address large defects encompassing conductor galloping damage and tower structural compromise. The architectural guarantee that each detection scale receives features informed by both cross-modal fusion semantics and multi-resolution spatial context establishes robust detection capability across the full spectrum of defect manifestations encountered in transmission-line inspection.

2.2. Semantic Recomposition Module

The Semantic Recomposition Module constitutes the foundational purification and enhancement mechanism deployed throughout the proposed network. As described in the architectural overview, SRM appears at multiple locations with differentiated configurations: compact-dictionary instances at branch P_3/P_4 levels perform intra-modal semantic purification, while large-dictionary instances at fused P_4/P_5 levels perform cross-modal semantic enhancement. This section elaborates the module’s internal design and explains how the unified encode-retrieve-normalize-decode mechanism serves these distinct functional roles.

SRM addresses a fundamental tension in multimodal feature processing: the need to suppress modality-specific noise while preserving discriminative details essential for detecting small-scale defects. Conventional approaches to feature refinements such as channel attention or spatial attention mechanisms are operate by reweighting existing feature activations, which limits their ability to introduce genuinely new information into the representation or to enforce explicit constraints on what constitutes valid semantic content. In contrast, SRM adopts a dictionary-based retrieval paradigm that projects input features into a learned semantic codebook, performs structured refinement within that space, and injects the retrieved information

back into the original representation through controlled residual mixing.

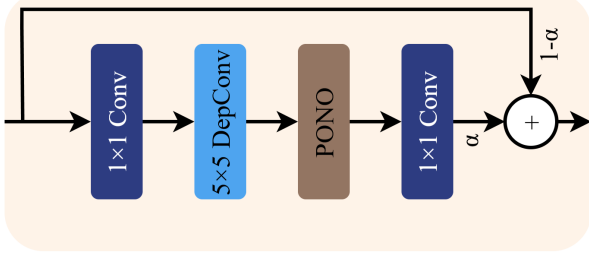


Figure 2: Architecture of the Semantic Recomposition Module. The input features are projected into a dictionary space via pointwise convolution, refined through depthwise spatial convolution, normalized at each spatial position (PONO denotes position-wise normalization), and decoded back to the original channel dimension. The output combines the refined features with the input through learnable residual mixing.

The architecture of SRM, illustrated in Fig. 2, implements a four-stage pipeline followed by residual injection. Given an input feature map $\mathbf{F} \in \mathbb{R}^{B \times C \times H \times W}$, the encoding stage projects it into a lower-dimensional dictionary space through a 1×1 pointwise convolution:

$$\mathbf{E} = \mathcal{P}_{\text{enc}}(\mathbf{F}), \quad \mathcal{P}_{\text{enc}} : \mathbb{R}^C \rightarrow \mathbb{R}^K, \quad (1)$$

where K denotes the dictionary size. This projection can be interpreted as computing soft assignment coefficients over a learned dictionary, with each spatial location in \mathbf{E} encoding how strongly the corresponding input feature aligns with each of the K dictionary atoms. The dictionary size K is deliberately set smaller than the input channel count C to encourage the network to learn a compact, semantically meaningful basis that captures essential structure while discarding irrelevant variations.

The retrieval stage aggregates spatial context within the dictionary space using a depthwise separable convolution with kernel size 5×5 :

$$\mathbf{R} = \mathcal{D}_{5 \times 5}(\mathbf{E}), \quad (2)$$

where $\mathcal{D}_{5 \times 5}$ operates independently on each dictionary channel without activation function. This design keeps the retrieval process close to an interpretable linear operation, aggregating information from local spatial neighborhoods for each atom while preventing nonlinearity from prematurely mixing noise with semantic information and spreading it across all channels. The enlarged kernel size ensures a receptive field sufficient to capture relationships between adjacent structural elements such as the spatial arrangement of insulator components or the linear continuity of transmission conductors while maintaining parameter efficiency through the depthwise formulation.

The normalization stage applies position-wise standardization across the dictionary dimension:

$$\mu_{h,w} = \frac{1}{K} \sum_{k=1}^K \mathbf{R}_{k,h,w}, \quad \sigma_{h,w} = \sqrt{\frac{1}{K} \sum_{k=1}^K (\mathbf{R}_{k,h,w} - \mu_{h,w})^2 + \epsilon}, \quad (3)$$

$$\hat{\mathbf{R}}_{k,h,w} = \frac{\mathbf{R}_{k,h,w} - \mu_{h,w}}{\sigma_{h,w}}, \quad (4)$$

where ϵ ensures numerical stability. Unlike batch normalization or layer normalization, which compute statistics over spatial or batch dimensions, position-wise normalization treats each spatial location independently. This design choice is motivated by the observation that different regions of a transmission-line image exhibit vastly different statistical properties background sky, metallic tower structures, and insulator assemblies each induce distinct activation patterns and imposing shared statistics across these heterogeneous regions would suppress meaningful variations. For cross-modal scenarios, this normalization proves particularly crucial: RGB and depth modalities produce systematically different response magnitudes and local variances at corresponding spatial positions, and position-wise normalization explicitly aligns these distributions before the features proceed to subsequent processing, preventing the network from learning shortcuts based on statistical differences rather than semantic content.

The decoding stage maps the normalized dictionary representation back to the original channel dimension through another 1×1 pointwise convolution:

$$\mathbf{D} = \mathcal{P}_{\text{dec}}(\hat{\mathbf{R}}), \quad \mathcal{P}_{\text{dec}} : \mathbb{R}^K \rightarrow \mathbb{R}^C. \quad (5)$$

This projection reconstructs a refined feature map by linearly recombining the normalized dictionary atoms according to learned coefficients, translating the purified semantic information back into the representation space expected by subsequent network layers.

The final output combines the refined features with the original input through residual mixing:

$$\mathbf{Y} = \alpha \cdot \mathbf{D} + (1 - \alpha) \cdot \mathbf{F}, \quad (6)$$

where the mixing coefficient $\alpha = 0.8$ allows the dictionary-refined component to dominate while preserving a direct pathway for fine-grained information essential to small-object localization. Complete reliance on reconstruction risks boundary detail erosion, while excessive preservation of original features fails to suppress modality noise effectively; this convex combination strikes the necessary balance.

The differentiated deployment of SRM across the network exploits the same mechanism for distinct purposes through dictionary capacity variation. At branch P_3/P_4 levels, the compact 128-atom dictionary creates an information bottleneck that forces features to be expressed using limited reusable primitives, effectively filtering out incidental noise and modality-private artifacts that cannot be stably reconstructed. This process creates a “reconstructable semantic subspace” for each modality, yielding features that are cleaner and more aligned in statistical properties before entering fusion. At fused P_4/P_5 levels, the enlarged 256-atom dictionary accommodates the greater complexity of the shared feature space while maintaining reconstructability-based selection: shared semantic patterns that project cleanly into dictionary space and normalize consistently receive strong reinforcement, while modality-private

residuals with inconsistent statistics receive attenuated injection. This mechanism transforms cross-modal alignment from implicit weight-based learning into explicit reconstruction-driven enhancement.

2.3. Contextual Semantic Integration Framework

While SRM effectively addresses intra-modal noise suppression and cross-modal distribution alignment through dictionary-based semantic purification, a fundamental limitation remains: the convolutional fusion operations at P_4 and P_5 levels operate within bounded receptive fields and consequently cannot capture long-range spatial dependencies. This limitation proves particularly problematic for transmission-line defect detection, where semantic interpretation frequently depends on global structural context. A damaged insulator, for instance, is more reliably identified when the network can reference the regular spatial arrangement of adjacent intact insulators to recognize deviation from expected patterns; similarly, foreign objects such as bird nests are distinguished from legitimate equipment by their inconsistency with the expected geometric layout of the transmission infrastructure. Without explicit mechanisms for global context modeling, the network must rely solely on local appearance cues that are often insufficient to disambiguate small defects from visually similar background elements.

To address this limitation, we introduce the Contextual Semantic Integration Framework (CSIF), deployed at the P_5 fusion stage where it serves to establish global contextual relationships among fused RGB-D features. The placement at P_5 reflects two design considerations: first, global attention is most valuable at deep semantic levels where features encode abstract concepts amenable to relational reasoning, whereas shallow features encoding fine-grained spatial details benefit more from local convolutional processing that preserves precise localization information; second, the computational cost of attention scales quadratically with spatial resolution, making the lowest-resolution P_5 scale the most tractable location for global modeling. However, directly applying standard Transformer-style attention to fused multimodal features introduces two subsidiary problems: full-channel global attention tends to cause detail erosion and over-smoothing that is particularly detrimental in small-object detection scenarios, and the concatenated RGB-depth features exhibit substantial distribution heterogeneity that standard layer normalization cannot adequately address. To resolve these issues, CSIF incorporates two specialized components: the Contextual Semantic Interaction Block (CSIB) implementing partial-channel attention with iterative refinement, and the Adaptive Semantic Regulation Mechanism (ASRM) providing structured normalization tailored for cross-modal feature distributions.

Fig. 3 illustrates the overall architecture of CSIF, which processes features through a “projectrefineproject” pipeline designed to balance global context acquisition with detail preservation. Given an input $\mathbf{X} \in \mathbb{R}^{B \times C_{in} \times H \times W}$ from the preceding fusion stage, CSIF produces a refined output $\mathbf{Z} \in \mathbb{R}^{B \times C_{out} \times H \times W}$. The convolutional stem transforms the input into an internal embedding suitable for attention computation, expanding the channel dimension by factor e to create sufficient capacity

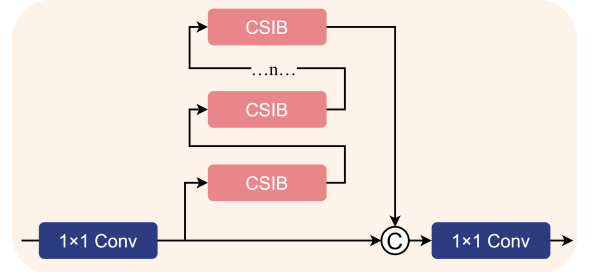


Figure 3: Architecture of the Contextual Semantic Integration Framework. The input features pass through a convolutional stem that harmonizes channel dimensions, followed by n stacked Contextual Semantic Interaction Blocks that perform attention-based global modeling with interleaved normalization. An output projection aligns the refined features to the target dimension.

for multi-head attention while harmonizing the heterogeneous statistics of the incoming concatenated RGB-D features. To prevent the detail erosion problem inherent in full-channel attention, CSIF adopts a partial-channel attention design: the stem output is split into two portions along the channel dimension, with only one portion passing through the attention block sequence while the other maintains a stable bypass. This design constrains strong global interaction to a subspace, preserving a direct semantic pathway that retains fine-grained information essential for small-object localization while simultaneously stabilizing gradient flow during training. The core refinement consists of n stacked CSIBs operating on the attention portion, with the iterative process formulated as $\mathbf{H}^{(i)} = \text{CSIB}(\mathbf{H}^{(i-1)})$ for $i = 1, \dots, n$, where $\mathbf{H}^{(0)}$ denotes the initial attention portion. After n iterations, the processed portion is concatenated with the bypassed portion, and an output projection maps the combined representation to the target channel dimension.

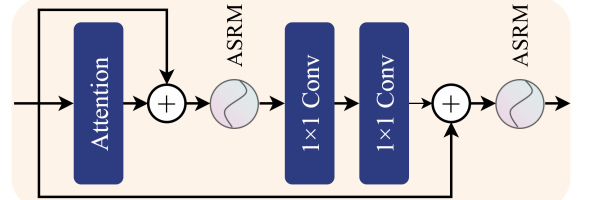


Figure 4: Structure of the Contextual Semantic Interaction Block. Each block comprises a multi-head self-attention layer followed by ASRM normalization, then a feed-forward network followed by another ASRM normalization. Residual connections facilitate gradient flow at both stages.

Within the partial-channel attention framework, a subsidiary problem arises: how to effectively model global dependencies while maintaining stable feature distributions across the attention and feed-forward stages. Standard Transformer blocks employ pre-normalization, but this arrangement proves inadequate for cross-modal fusion scenarios where the concatenated RGB and depth features exhibit persistent distribution heterogeneity that channel-wise standardization alone cannot fully resolve. To address this problem, the Contextual Semantic Interaction Block adopts post-normalization placement with specialized ASRM modules that provide distribution-aware regularization. As shown in Fig. 4, each CSIB implements a two-phase cycle

of attention and feed-forward transformation. The first phase applies multi-head self-attention to capture global spatial dependencies:

$$\mathbf{Q} = \mathbf{HW}_Q, \quad \mathbf{K} = \mathbf{HW}_K, \quad \mathbf{V} = \mathbf{HW}_V, \quad (7)$$

$$\text{Attn}(\mathbf{H}) = \text{softmax}\left(\frac{\mathbf{Q}\mathbf{K}^\top}{\sqrt{d_k}}\right)\mathbf{V}, \quad (8)$$

where $\mathbf{W}_Q, \mathbf{W}_K, \mathbf{W}_V$ are learnable projection matrices and d_k is the dimension per attention head. The number of heads adapts to the channel configuration as $h = \max(1, \lfloor C/64 \rfloor)$ to ensure stable attention computation across varying feature dimensions. A residual connection preserves input information: $\mathbf{U} = \mathbf{H} + \text{Attn}(\mathbf{H})$. Following attention, ASRM normalizes the feature distribution while preserving semantically relevant variations: $\hat{\mathbf{U}} = \text{ASRM}_1(\mathbf{U})$. The second phase applies a feed-forward network for nonlinear feature transformation:

$$\text{FFN}(\hat{\mathbf{U}}) = \mathbf{W}_2 \cdot \sigma(\mathbf{W}_1 \hat{\mathbf{U}} + \mathbf{b}_1) + \mathbf{b}_2, \quad (9)$$

followed by another residual connection and ASRM normalization: $\mathbf{V} = \hat{\mathbf{U}} + \text{FFN}(\hat{\mathbf{U}})$, $\mathbf{H}^{(i)} = \text{ASRM}_2(\mathbf{V})$. The placement of normalization after both attention and FFN stages ensures that the persistent distribution heterogeneity of cross-modal features is explicitly addressed before the FFN amplifies any distributional artifacts through its nonlinear transformations.

The Adaptive Semantic Regulation Mechanism is introduced to stabilize feature distributions and regulate semantic magnitudes after global semantic interactions. In cross-modal fusion scenarios, global interactions such as self-attention and feed-forward transformations tend to amplify distributional discrepancies between heterogeneous semantic subspaces, which may result in feature drift and over-smoothing. ASRM addresses this issue by providing a controlled and learnable mechanism that balances distribution regularization with semantic preservation. Let the input feature be denoted as $\mathbf{x} \in \mathbb{R}^{B \times C \times H \times W}$. Rather than enforcing hard normalization, ASRM constructs a learnable semantic regulation gate that interpolates between the normalized representation and the original feature:

$$\tilde{\mathbf{x}} = \gamma \odot \text{LN}(\mathbf{x}) + \gamma_x \odot \mathbf{x}, \quad (10)$$

where $\text{LN}(\cdot)$ denotes channel-wise layer normalization, $\gamma, \gamma_x \in \mathbb{R}^{C \times 1 \times 1}$ are learnable scaling parameters, and \odot represents the Hadamard product. This formulation ensures that normalization contributes to representation learning in a regulated manner, instead of overriding the original semantic structure. On top of the regulated feature $\tilde{\mathbf{x}}$, ASRM applies a constrained semantic adaptation mapping $\mathcal{F}(\cdot)$, which operates in a low-dimensional semantic subspace and injects the adapted information back to the original feature space via a residual formulation:

$$\mathbf{y} = \mathbf{x} + \mathcal{F}(\tilde{\mathbf{x}}). \quad (11)$$

Through this residual semantic injection, ASRM confines global semantic corrections to a controlled subspace, preventing disruptive modifications to the backbone representation while still enabling effective regulation.

From an optimization perspective, ASRM exhibits progressive regulation behavior. By initializing γ to near-zero values and γ_x to unity, the mechanism approximates an identity mapping at early training stages, i.e., $\tilde{\mathbf{x}} \approx \mathbf{x}$, which avoids premature interference with unstable global attention patterns. As training proceeds, the learnable parameters adaptively increase the influence of the normalization branch, enabling a smooth transition from weak to strong semantic regulation. This progressive nature is particularly beneficial in cross-modal settings where the coupling between attention weights and normalization statistics requires gradual calibration. Conceptually, ASRM serves as a re-anchoring mechanism for global semantic updates: while self-attention captures long-range and cross-modal dependencies, ASRM constrains their impact through regulated normalization and residual semantic correction, ensuring that global context modeling enhances rather than obscures fine-grained discriminative cues. As a result, ASRM establishes a stable balance between global semantic coherence and local detail sensitivity, providing robust high-level representations for subsequent detection modules.

In the proposed architecture, CSIF with $n = 2$ CSIB blocks operates at the P_5 fusion level. The hierarchical design with partial-channel attention preventing detail erosion, CSIB providing stable attention-FFN cycles through post-normalization, and ASRM enabling smooth normalization transition with progressive semantic regulation collectively achieves the goal of global context modeling without sacrificing the fine-grained discrimination essential for small-object detection. The integration of CSIF at this fusion stage addresses the fundamental limitation of concatenation-based multimodal fusion: while concatenation preserves all information from both modalities, it provides no mechanism for establishing correspondence relationships between RGB-derived and depth-derived feature channels. The global attention computation within CSIF enables direct interaction between features originating from different modalities, learning which RGB patterns should attend to which depth patterns for optimal defect representation. This cross-modal attention emerges implicitly through end-to-end training, as the detection loss gradient encourages attention patterns that support accurate classification and localization of transmission-line defects. The refined P_5 features subsequently pass through SRM for dictionary-based enhancement, ensuring that both global context coherence from CSIF and reconstructability-based reinforcement from SRM contribute to the semantic representations that propagate through the detection head.

3. Experiments

3.1. Datasets

This study employs the TL-RGBD (Transmission Line RGB-D Dataset), a large-scale, high-resolution RGB-D dataset specifically designed for detecting defects in power transmission line components. The dataset comprises 10,000 paired RGB and depth images of insulators, tie wires, and poles, captured under authentic inspection scenarios by China Southern Power Grid using UAVs equipped with synchronized RGB

cameras and depth sensors. The depth information, acquired directly through onboard depth cameras during flight missions, provides complementary geometric and spatial information crucial for precise defect localization.

Each image pair (RGB and depth) was annotated by domain experts with bounding boxes and category labels, ensuring high-quality and consistent labeling. The dataset encompasses 73,448 annotated instances across nine component states and defect types, as detailed in Table 1.

Table 1: Correspondence between labels and category names.

No.	Label	Category name
1	zcjyz	Normal insulator
2	jyzwh	Polluted insulator
3	dgss	Damaged pole
4	zxqs	Missing tie wire
5	zxst	Loose tie wire
6	jyzsl	Insulator flashover
7	nw	Bird nest
8	jyzps	Broken insulator
9	zyzsl	Shattered post insulator

The TL-RGBD dataset exhibits several distinctive characteristics that reflect the intrinsic challenges of UAV-based transmission line inspection. Statistical analysis reveals a highly imbalanced distribution of object sizes, with each annotated object occupying an average area of 422.12 pixels. The dataset composition demonstrates an extreme dominance of small-scale targets: 94.51% are classified as small objects (69,413 instances with area $< 32^2$ pixels), 5.48% as medium-sized objects (4,022 instances with $32^2 \leq \text{area} < 96^2$ pixels), and merely 0.02% as large objects (13 instances with area $\geq 96^2$ pixels). This extreme skew toward small-scale targets poses significant challenges for detection algorithms and accurately represents real-world inspection scenarios where defects often manifest as subtle, localized anomalies.

The depth maps, captured synchronously with RGB images using onboard depth sensors, provide critical geometric cues that complement RGB appearance features. Depth data proves particularly valuable for distinguishing between visually similar defects, identifying component protrusions or deformations, measuring geometric anomalies, and improving localization accuracy under challenging illumination conditions where RGB information alone may be insufficient. This multimodal approach enables more robust defect characterization by leveraging both photometric and geometric properties of transmission line components.

In summary, the TL-RGBD dataset with native RGB-D modalities provides a robust, high-fidelity benchmark that advances both domain-specific defect detection research and general small-object detection methodologies in aerial remote sensing applications. The combination of authentic inspection data with synchronized depth sensing offers enhanced domain relevance and addresses challenging detection scenarios specific to critical infrastructure monitoring.

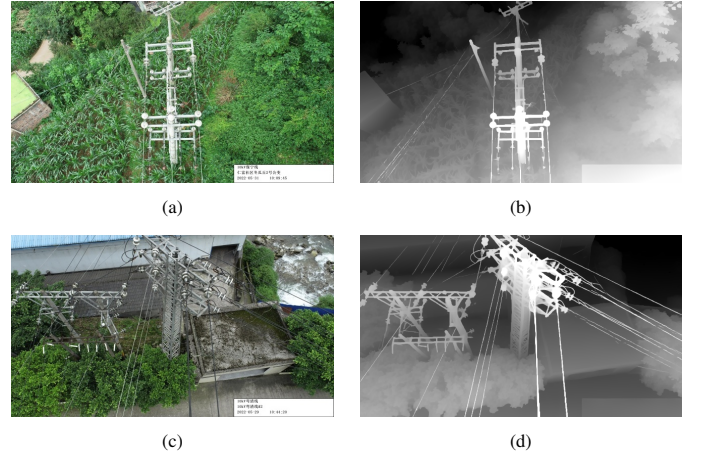


Figure 5: Sample image pairs from TL-RGBD dataset. (a) and (c) are RGB images captured by UAV-mounted cameras showing transmission line components under real inspection conditions. (b) and (d) are the corresponding depth maps acquired synchronously, providing geometric information for defect localization.

3.2. Model Training and Evaluation Metrics

The proposed cross-modal alignment and fusion network was implemented using the PyTorch framework (version 2.3.1). All experiments were conducted on a workstation equipped with an NVIDIA GeForce RTX 3090 GPU (24 GB memory) running Ubuntu 22.04 LTS with CUDA 12.1 and Python 3.10.14.

Model performance was assessed on the held-out test set following the standard COCO evaluation protocol. We report two primary metrics: mAP_{50} , which measures mean average precision at an intersection-over-union (IoU) threshold of 0.50, and $\text{mAP}_{50:95}$, which averages precision across IoU thresholds ranging from 0.50 to 0.95 in increments of 0.05.

Given the prevalence of small-scale defects in transmission-line inspection scenarios captured by UAV-mounted RGB-D sensors, we additionally report scale-sensitive metrics defined by the COCO protocol: AP_s for small objects (area $< 32^2$ pixels) and AP_m for medium objects (area between 32^2 and 96^2 pixels). The AP_s metric is particularly informative for assessing the model’s capability to detect fine-grained, low-pixel-count anomalies, a critical requirement for reliable transmission-line monitoring. Computational efficiency and model complexity were quantified using floating-point operations (FLOPs) and the total number of parameters (Params, in millions). Detection performance was evaluated through precision (P), recall (R), average precision (AP), and mean average precision (mAP), defined as follows:

$$P = \frac{TP}{TP + FP}, \quad R = \frac{TP}{TP + FN},$$

where TP , FP , and FN denote true positives, false positives, and false negatives, respectively. For each defect category, average precision is computed as the area under the precision-recall curve:

$$\text{AP} = \int_0^1 P(R) dR,$$

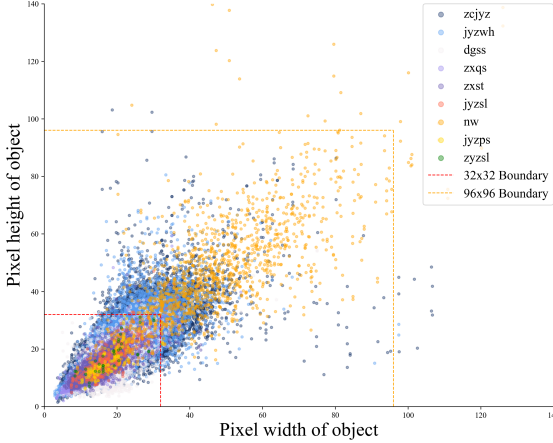


Figure 6: Distribution of object sizes in the TL-RGBD dataset. The scatter plot shows the pixel width and height of all annotated instances after preprocessing, with different colors representing distinct defect categories. The concentration of points in the lower-left region indicates the predominance of small-scale objects. Dashed lines at 32×32 and 96×96 pixels mark the boundaries between small, medium, and large object categories.

and mean average precision across k categories is given by:

$$\text{mAP} = \frac{1}{k} \sum_{i=1}^k \text{AP}_i.$$

Collectively, these computational metrics (FLOPs, Params) and detection metrics (mAP, scale-sensitive AP) provide a balanced evaluation of accuracy, completeness, and operational efficiency for RGB-D sensor-based transmission-line defect detection.

3.3. Model Scaling Strategy

The proposed CMAFNet architecture adopts a unified scaling paradigm that enables systematic adaptation across diverse deployment scenarios without modifying the underlying network topology. Following the compound scaling methodology established in modern detection frameworks, the architecture defines five capacity configurations—nano (n), small (s), medium (m), large (l), and extra-large (x)—through coordinated adjustment of two scaling coefficients: *depth_multiple*, which governs the repetition count of stackable blocks within each stage, and *width_multiple*, which controls the channel dimensionality at each layer. An additional *max_channels* parameter imposes an upper bound on deep-layer channel expansion to prevent computational overhead from scaling superlinearly in dual-branch fusion architectures. This parameterization produces a family of models sharing identical architectural topology and module composition, differing only in representational capacity and computational cost.

The scaling coefficients for the five configurations are specified as follows: CMAFNet-n employs [depth = 0.50, width = 0.25, *max_channels* = 1024], CMAFNet-s uses [0.50, 0.50, 1024], CMAFNet-m adopts [0.50, 1.00, 512], CMAFNet-l applies [1.00, 1.00, 512], and CMAFNet-x employs [1.00, 1.50, 512]. These configurations establish a progressive capacity gradient spanning from 4.9M parameters and

12.4 GFLOPs at the nano scale to 100.7M parameters and 337.4 GFLOPs at the extra-large scale, while maintaining inference speeds ranging from 227.6 FPS to 62.6 FPS on standard GPU hardware. The transitions between adjacent scales embody distinct capacity expansion strategies: $n \rightarrow s$ increases channel width while preserving depth, thereby expanding feature dimensionality for richer local representations; $s \rightarrow m$ further widens channels to baseline capacity while introducing deep-layer channel capping to constrain fusion-stage computation; $m \rightarrow l$ restores full block repetition counts to enhance hierarchical abstraction depth; $l \rightarrow x$ extends mid-to-high-level channel width beyond baseline under continued deep-layer capping, maximizing cross-modal fusion capacity.

The rationale for incorporating the *max_channels* constraint merits particular attention in the context of dual-branch RGB-D architectures. Unlike single-stream detectors where channel expansion propagates uniformly through the network, the proposed fusion strategy concatenates features from parallel branches at P_4 and P_5 scales, effectively doubling the channel count at fusion points before subsequent compression. Without explicit bounds, applying large width multipliers would cause deep-layer channels to exceed practical memory limits, particularly at the P_5 fusion stage where the Contextual Semantic Integration Framework performs global attention operations with quadratic memory complexity in channel dimension. The *max_channels* parameter set to 512 for medium through extra-large configurations ensures that fusion-stage channels remain tractable while permitting aggressive width expansion at shallower scales where cross-modal concatenation has not yet occurred.

The selection of an appropriate model scale should be guided by a hierarchical decision framework that prioritizes task-side constraints over deployment-side constraints when both are applicable. Transmission-line defect detection presents a canonical example of task-driven scaling requirements: with 94.51% of annotated instances in the TL-RGBD dataset classified as small objects under COCO criteria, the detection task demands high-capacity models capable of preserving fine-grained features through deep pyramid pathways while accommodating the expanded representational requirements of cross-modal fusion. Small targets impose stringent demands on feature resolution and semantic granularity—characteristics that lightweight models struggle to maintain as features propagate through successive downsampling and fusion operations. Consequently, when the application domain exhibits predominant small-object distributions or requires high localization precision for subtle defects, the recommended configuration corresponds to large or extra-large scales regardless of available computational resources.

When task-side constraints do not unambiguously dictate capacity requirements—for instance, in scenarios involving mixed object scales or moderate precision tolerances—the deployment platform becomes the primary determinant of model selection. Edge devices such as UAV-mounted inference units or embedded processors impose severe constraints on power consumption, memory bandwidth, and computational throughput, necessitating the nano configuration to achieve stable real-

time inference despite moderate accuracy reduction. Mobile computing platforms including portable inspection terminals and field workstations offer intermediate computational capacity, rendering the small configuration appropriate for balancing responsiveness with detection fidelity. Desktop GPUs and server-class accelerators provide sufficient resources to support medium through extra-large configurations, with the specific choice determined by latency requirements and offline versus real-time operational modes. For batch processing of archived inspection imagery where throughput rather than latency governs efficiency, the extra-large configuration maximizes detection accuracy without deployment constraints.

This task-platform scaling framework produces consistent model selection across application scenarios: small-object-dominated tasks direct selection toward high-capacity configurations, while resource-constrained deployments direct selection toward lightweight configurations. The framework resolves potential conflicts by assigning precedence to task requirements—if small-object detection mandates high capacity but edge deployment requires low complexity, practitioners must either accept reduced accuracy on edge platforms or migrate inference to more capable hardware. The experimental results presented in Table 2 validate this framework empirically: CMAFNet-x achieves the highest AP_s of 0.125 on the small-object-dominated TL-RGBD dataset, representing a 38.9% relative improvement over CMAFNet-n, while CMAFNet-n maintains competitive mAP_{50} of 0.248 at 227.6 FPS for latency-critical deployments. The monotonic relationship between model capacity and small-object performance across all five scales confirms that the scaling strategy successfully translates architectural capacity into detection capability for the target application domain.

3.4. Comparisons With Previous Methods

We benchmark CMAFNet against state-of-the-art object detection methods spanning three architectural paradigms: CNN-based single-stage detectors from the YOLO family (v5, v8, v10, v11), transformer-based end-to-end detectors built on the DETR framework (RT-DETR, Conditional-DETR, DETR, DINO), and a specialized small-object detector (FFCA-YOLO). Additionally, we compare against TinyDef-DETR, a domain-specific transformer tailored for transmission-line defect detection. For RGB-only baselines, we adopt results from our prior work (Shen et al., 2025), ensuring identical dataset splits and training configurations for fair comparison.

Table 2 presents the quantitative results on the TL-RGBD dataset. CMAFNet-x achieves the highest mAP_{50} of 0.322, surpassing the best-performing baseline DINO (0.224) by 9.8 percentage points. This superiority persists across all model scales: CMAFNet-n attains an mAP_{50} of 0.248 with only 4.9M parameters and 12.4 GFLOPs, outperforming all YOLO variants and matching larger transformer models. Such scaling behavior indicates that the performance gains stem primarily from cross-modal fusion rather than increased model capacity. For small-object detection—the core challenge in transmission-line imagery—CMAFNet-x achieves an AP_s of 0.125, improving upon DINO (0.085) by 4.0 percentage points and substan-

tially exceeding YOLO variants (0.06–0.08). The $mAP_{50:95}$ metric further confirms this advantage: CMAFNet-x reaches 0.147 versus 0.099 for DINO and 0.072–0.083 for leading YOLO configurations, demonstrating that cross-modal fusion enhances both detection recall and boundary localization. Although large objects constitute merely 0.02% of the TL-RGBD dataset (13 instances with area $\geq 96^2$ pixels), we report AP_l for completeness; notably, even the smallest variant CMAFNet-n achieves 0.369 on this subset, establishing a lower bound that larger configurations are expected to exceed. Category-specific metrics for $jywh$ and $dgss$ —the two most prevalent defect types in the TL-RGBD dataset—reveal pronounced improvements: CMAFNet-x achieves a recall of 0.584 and mAP_{50} of 0.517 for $jywh$ defects (DINO: 0.437 and 0.420), and 0.463 recall with 0.465 mAP_{50} for $dgss$ defects (DINO: 0.402 and 0.426). These results validate that depth modality provides discriminative geometric cues complementing RGB appearance features, particularly for defects with subtle visual signatures but distinctive three-dimensional profiles.

Analysis of baseline methods reveals distinct performance patterns across architectural paradigms. Among YOLO detectors, scaling model capacity yields only marginal mAP_{50} improvements of 0.02–0.04 despite substantial increases in parameters and computation. For instance, YOLOv8m (23.2M parameters, 67.5 GFLOPs) achieves an mAP_{50} of 0.163, only 0.030 higher than YOLOv8n (2.7M parameters, 6.8 GFLOPs). This saturation suggests that RGB features alone provide limited discriminative power for small, visually ambiguous defects, and that increased network capacity cannot overcome this inherent modality limitation. YOLOv11s-P2, incorporating an additional high-resolution detection head for small objects, achieves the best YOLO performance ($mAP_{50} = 0.181$), yet remains substantially below CMAFNet-n despite comparable computational cost. Transformer-based detectors achieve higher accuracy than YOLO counterparts—DINO reaches 0.224 mAP_{50} and RT-DETR-x reaches 0.216—indicating that global attention mechanisms offer advantages for capturing contextual relationships among spatially distributed defects. However, RT-DETR-x requires 222.5 GFLOPs, approximately 33× that of YOLOv8n, and performance varies inconsistently across backbones: RT-DETR-R50 (0.115 mAP_{50}) underperforms RT-DETR-R18 (0.163 mAP_{50}), revealing sensitivity to backbone selection in this domain. FFCA-YOLO, designed specifically for small-object detection, achieves only 0.142 mAP_{50} and 0.059 AP_s , underscoring that methods optimized for generic small-object scenarios may not transfer effectively to transmission-line imagery where targets exhibit both small scale and low visual contrast against complex backgrounds.

Comparison with TinyDef-DETR (Shen et al., 2025), representing the prior state-of-the-art for transmission-line defect detection, further demonstrates the effectiveness of cross-modal fusion. Despite TinyDef-DETR’s domain-specific architectural refinements, CMAFNet-x achieves superior performance across all metrics, indicating that geometric cues from depth imagery—when properly aligned—provide discriminative information that single-modal architectural innovations cannot capture. The lightweight CMAFNet-n attains comparable accu-

Table 2: Comprehensive performance comparison of different object detection models on the TL-RGBD dataset. The best results are highlighted in bold.

Model	Epochs	Params(M)	GFLOPs	P	R	mAP ₅₀	mAP _{50:95}	AP _s	AP _m	FPS	Recall _{jyzwh}	Recall _{dgss}	mAP ₅₀ ^{jyzwh}	mAP ₅₀ ^{dgss}
YOLO v5n	300	2.2	5.8	0.707	0.131	0.131	0.063	0.061	0.097	243.9	0.352	0.292	0.315	0.258
YOLO v5s	300	9.1	23.8	0.346	0.148	0.140	0.065	0.065	0.098	181.8	0.377	0.323	0.314	0.270
YOLO v5m	300	25.1	64.0	0.548	0.164	0.162	0.072	0.079	0.081	74.6	0.372	0.321	0.367	0.277
YOLO v8n	300	2.7	6.8	0.580	0.134	0.133	0.061	0.066	0.078	263.2	0.364	0.303	0.321	0.264
YOLO v8s	300	11.1	28.5	0.375	0.155	0.147	0.066	0.067	0.095	147.1	0.388	0.321	0.331	0.269
YOLO v8m	300	23.2	67.5	0.403	0.169	0.163	0.072	0.075	0.087	66.2	0.378	0.328	0.360	0.296
YOLO v10n	300	2.7	8.2	0.707	0.125	0.133	0.063	0.062	0.094	270.3	0.352	0.237	0.321	0.251
YOLO v10s	300	8.0	24.5	0.536	0.144	0.157	0.073	0.078	0.095	140.8	0.343	0.288	0.341	0.308
YOLO v10m	300	16.6	63.5	0.386	0.170	0.162	0.075	0.075	0.097	67.1	0.390	0.361	0.356	0.294
YOLO v11n	300	2.6	6.3	0.638	0.135	0.136	0.064	0.060	0.103	263.2	0.353	0.274	0.324	0.245
YOLO v11s	300	9.4	21.3	0.516	0.166	0.155	0.072	0.074	0.100	125.0	0.381	0.314	0.344	0.291
YOLO v11s-P2	300	9.6	28.7	0.608	0.183	0.181	0.083	0.087	0.100	99.0	0.384	0.326	0.366	0.323
YOLO v11m	300	20.0	67.7	0.399	0.181	0.173	0.078	0.082	0.094	65.8	0.382	0.358	0.373	0.307
RT-DETR-1	100	32.8	108.0	0.480	0.189	0.199	0.089	0.078	0.044	38.5	0.360	0.337	0.341	0.372
RT-DETR-x	100	65.5	222.5	0.485	0.199	0.216	0.099	0.083	0.058	14.9	0.366	0.371	0.363	0.403
RT-DETR-R18	100	19.8	57.0	0.369	0.177	0.163	0.074	0.071	0.039	88.0	0.347	0.381	0.316	0.354
TinyDef-DETR	100	20.5	65.3	0.534	0.263	0.275	0.119	0.106	0.110	62.8	0.397	0.356	0.391	0.419
RT-DETR-R34	100	31.2	88.8	0.354	0.127	0.117	0.053	0.056	0.062	61.1	0.293	0.338	0.260	0.284
RT-DETR-R50	100	42.9	134.8	0.363	0.120	0.115	0.051	0.054	0.027	36.5	0.278	0.292	0.254	0.275
RT-DETR-R101	100	74.7	247.1	0.467	0.185	0.193	0.088	0.073	0.050	25.6	0.345	0.367	0.316	0.378
Conditional-DETR-R18	50	—	—	0.309	0.068	0.038	0.011	0.009	0.016	—	0.150	0.111	0.073	0.082
Conditional-DETR-R34	50	—	—	0.447	0.082	0.034	0.009	0.006	0.011	—	0.184	0.123	0.063	0.059
Conditional-DETR-R50	50	44.0	89.5	0.568	0.159	0.172	0.066	0.064	0.057	41.1	0.406	0.294	0.389	0.287
DETR-R50	500	—	—	0.301	0.138	0.124	0.043	0.041	0.037	—	0.289	0.258	0.280	0.203
DINO	12	—	—	0.496	0.257	0.224	0.099	0.085	0.075	—	0.437	0.402	0.420	0.426
FFCA-YOLO	300	7.1	51.4	0.680	0.130	0.142	0.060	0.059	0.051	50.8	0.286	0.291	0.291	0.270
CMAFNet-n	300	4.9	12.4	0.486	0.240	0.248	0.109	0.090	0.071	227.6	0.450	0.349	0.438	0.396
CMAFNet-s	300	19.7	41.8	0.502	0.281	0.270	0.121	0.099	0.068	188.6	0.496	0.420	0.456	0.420
CMAFNet-m	300	33.8	118.1	0.420	0.290	0.291	0.132	0.110	0.075	126.8	0.529	0.402	0.490	0.441
CMAFNet-l	300	42.3	149.8	0.574	0.302	0.307	0.141	0.113	0.066	96.5	0.537	0.431	0.505	0.451
CMAFNet-x	300	94.3	332.2	0.418	0.342	0.322	0.147	0.125	0.073	62.6	0.584	0.463	0.517	0.465

racy to TinyDef-DETR with fewer parameters, suggesting that cross-modal fusion offers a more efficient pathway to improved detection than scaling single-modal complexity.

Fig. 7 presents qualitative comparisons on four representative test samples containing densely distributed small-scale defects. Each sample is cropped to focus on high defect concentration regions, with detection results rendered as filled regions for visual clarity. CMAFNet consistently produces more complete and spatially coherent detections. DINO tends to generate fragmented predictions when multiple defects appear in close proximity, as evidenced by incomplete coverage in rows (b) and (c)—likely due to the global attention mechanism’s difficulty in resolving fine-grained spatial boundaries without explicit depth guidance. RT-DETR-R18 exhibits pronounced false negatives, missing substantial small targets across all scenes due to relatively coarse feature resolution at the detection head. YOLOv5s achieves reasonable coverage on larger defects but struggles with the smallest instances, producing noticeably lower recall in high-density regions. In contrast, CMAFNet maintains robust performance across varying object scales and spatial densities, yielding predictions closely aligned with ground-truth annotations. These visual observations corroborate the quantitative findings and suggest that cross-modal fusion leverages complementary geometric cues from depth imagery to compensate for ambiguities inherent in RGB-only representations.

Fig. 8 visualizes the accuracy-complexity trade-off across all

evaluated methods. YOLO-based methods cluster in the lower-left region with high inference speed but limited accuracy, while transformer-based methods occupy the upper-right with higher accuracy but disproportionately large computational requirements. CMAFNet variants trace a favorable trajectory through the upper portion, achieving accuracy comparable to or exceeding the largest transformer models while maintaining parameters and GFLOPs closer to mid-sized YOLO detectors. From an inference perspective, CMAFNet-n achieves 227.6 FPS with an mAP₅₀ of 0.248, suitable for real-time deployment on resource-constrained UAV platforms. CMAFNet-x maintains 62.6 FPS—substantially faster than RT-DETR-x (14.9 FPS) and RT-DETR-1 (38.5 FPS)—while achieving markedly higher accuracy.

Fig. 9 presents a radar-chart visualization profiling eight normalized performance indicators: overall recall, mAP₅₀, mAP_{50:95}, AP_s, inference speed, and category-specific metrics for jyzwh and dgss defects. YOLO-based methods exhibit elongated profiles extending toward the FPS axis, reflecting optimization for speed at the expense of accuracy. Transformer-based methods display more balanced but smaller profiles, with contracted regions along the FPS axis indicating computational intensity. CMAFNet exhibits the largest enclosed area among all methods, with pronounced expansion along recall, mAP, and category-specific axes while maintaining competitive inference speed. This comprehensive profiling confirms that CMAFNet

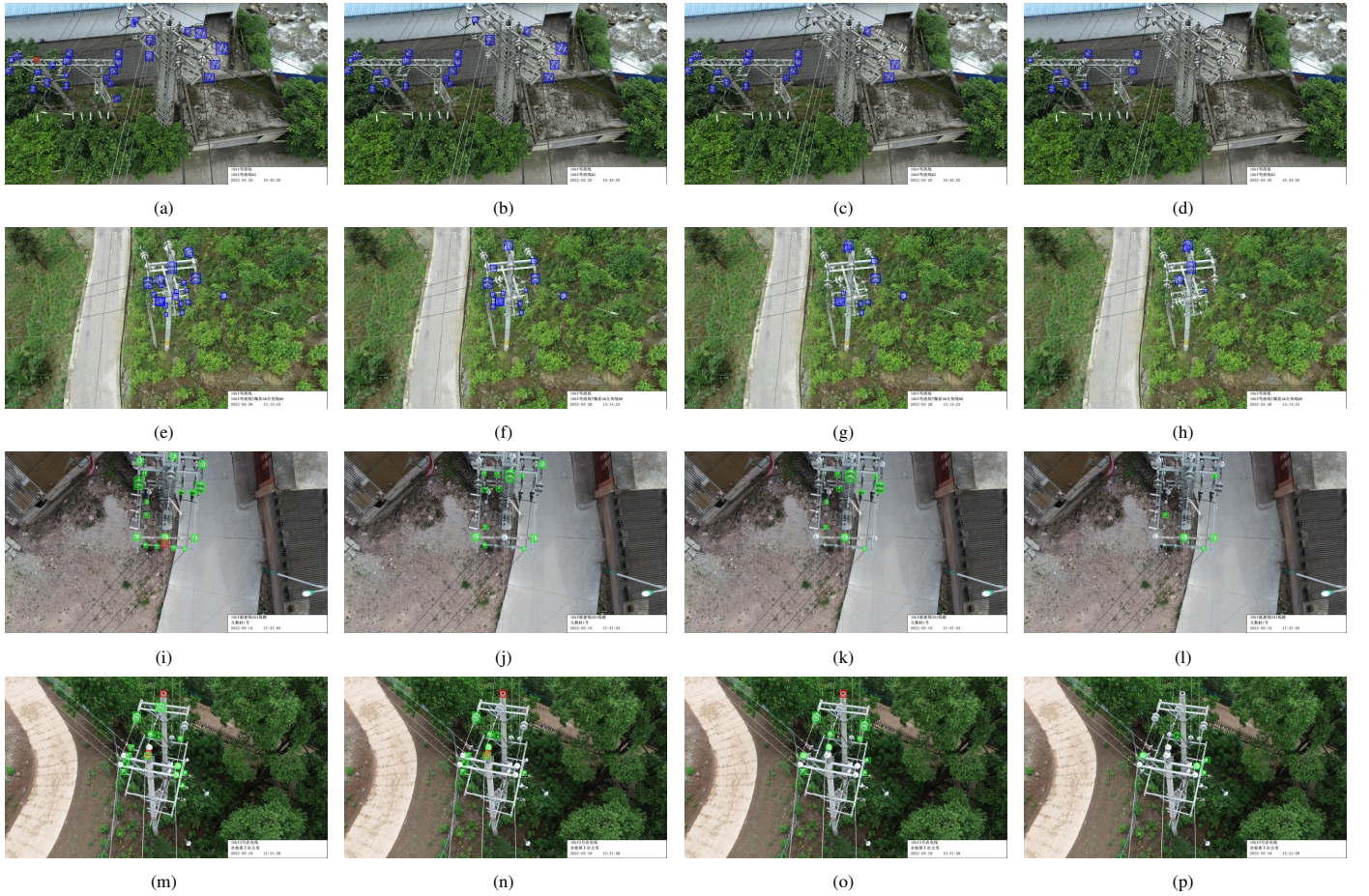


Figure 7: Qualitative comparison of detection results on four representative test samples. Each row corresponds to a different scene, and columns from left to right show predictions from CMAFNet, DINO, RT-DETR-R18, and YOLOv5s, respectively. Detection outputs are rendered as filled regions to facilitate visual discrimination under dense object distributions.

offers superior and well-balanced performance across diverse evaluation dimensions, validating cross-modal alignment and fusion as an effective strategy for RGB-D transmission-line defect detection.

3.5. Visualization Analysis via Feature Heatmaps

To provide intuitive insight into how the proposed modules influence feature learning, we visualize activation heatmaps extracted from the $P_3/8$ -small detection layer, which is responsible for detecting the smallest defects in the multi-scale detection head. Fig. 10 presents a representative comparison between the baseline model (without SRM and CSIF) and the complete CMAFNet architecture.

The baseline model without SRM and CSIF exhibits diffuse activation patterns that spread across extensive background regions, including tower lattice structures, sky areas, and conductor segments without defects. This scattered attention distribution reflects the network's inability to distinguish semantically relevant regions from visually similar but non-defective areas when lacking the dictionary-based purification and global context modeling mechanisms. The unfocused activations lead to two detrimental consequences: genuine defect regions receive

insufficient attention weight relative to their surroundings, increasing the likelihood of missed detections, while irrelevant background regions accumulate spurious activations that contribute to false positive predictions.

In contrast, the complete CMAFNet with SRM and CSIF produces markedly different activation characteristics. The heatmap demonstrates spatially concentrated activation patterns that align closely with actual defect locations, exhibiting both precise localization and comprehensive coverage of target regions. Several distinguishing features merit attention. First, the activation intensity peaks sharply at defect centers while decaying rapidly toward surrounding background, indicating that the network has learned to discriminate defect boundaries with high spatial precision. Second, the activation coverage extends across the full spatial extent of each defect rather than fragmenting into disconnected patches, suggesting that the global context modeling in CSIF enables the network to perceive defects as coherent semantic entities rather than isolated local patterns. Third, background suppression is substantially enhanced, with tower structures, conductors, and sky regions exhibiting minimal activation despite their visual prominence in the input image.

These visualization results corroborate the quantitative find-

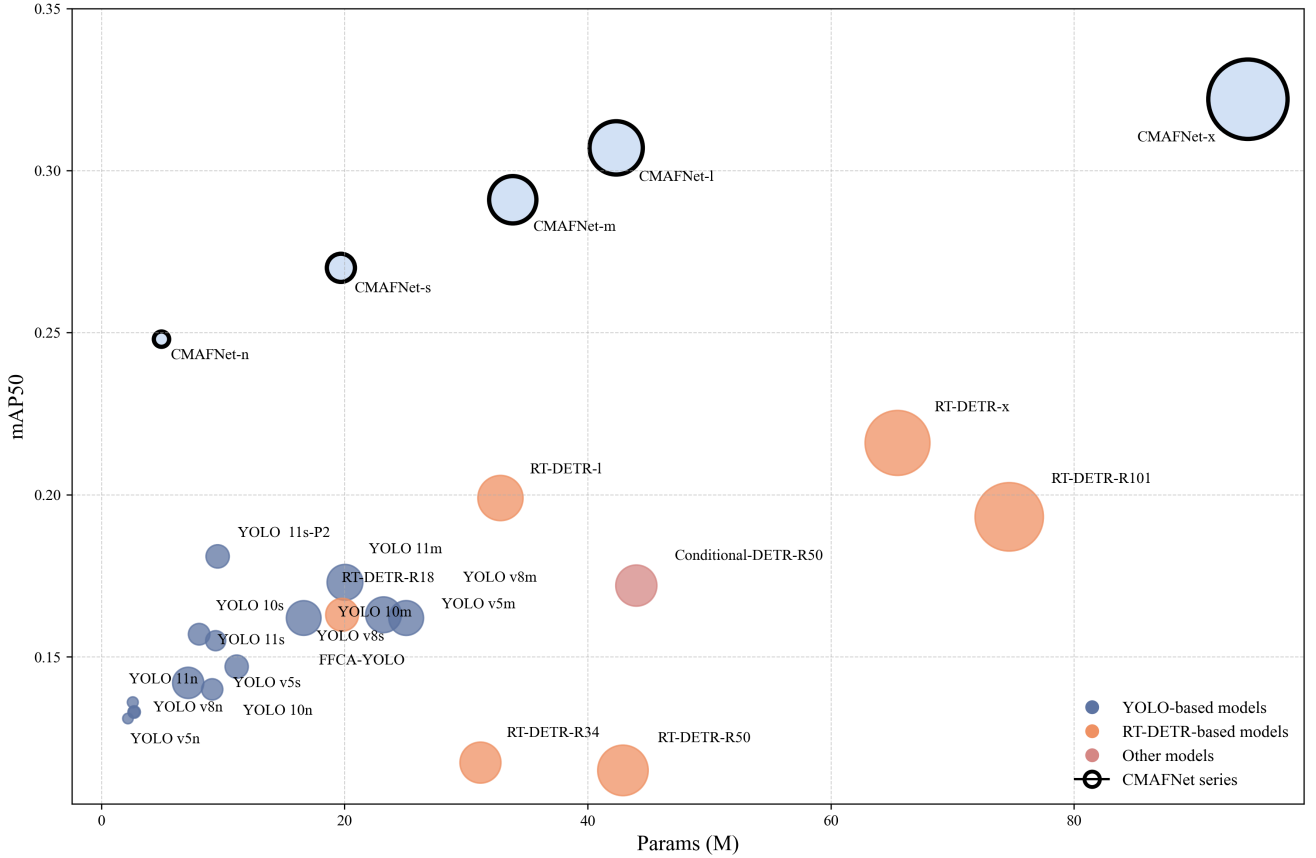


Figure 8: Accuracy-complexity trade-off visualization. The horizontal axis denotes parameters (millions), the vertical axis represents mAP₅₀, and bubble area is proportional to GFLOPs. CMAFNet variants are highlighted with black boundaries.

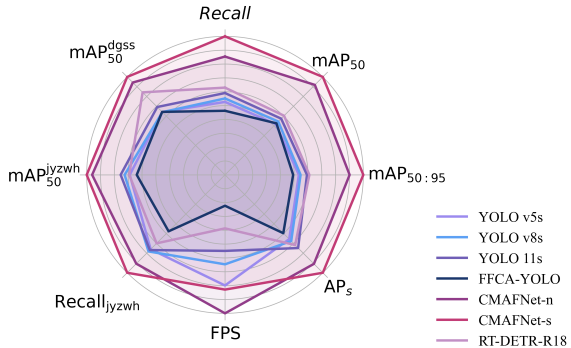


Figure 9: Multi-dimensional performance profiling via radar chart. Eight normalized indicators are visualized, with larger enclosed areas indicating more balanced detection capability.

ings from the ablation study and illuminate the underlying mechanisms through which SRM and CSIF improve detection performance. The dictionary-based semantic recomposition in SRM projects features into a normalized space where modality-specific noise and incidental textures are suppressed, enabling cleaner semantic representations that activate more selectively on genuine defect patterns. Simultaneously, the global attention mechanism in CSIF establishes long-range contextual relationships that help the network distinguish defects from structurally

similar but semantically distinct background elements by referencing the expected spatial arrangements of transmission-line components. The combined effect manifests as the focused, target-aligned activation patterns observed in the visualization, providing interpretable evidence that the proposed modules successfully guide the network toward more discriminative feature learning for small defect detection in complex transmission-line imagery.

3.6. Ablation Study

This section evaluates the contribution of each proposed module through controlled ablation experiments. We progressively remove the Semantic Recomposition Module (SRM) and the Cross-modal Semantic Interaction Fusion (CSIF) from the complete CMAFNet architecture, with results summarized in Table 3. To reduce training time and computational resource consumption, all ablation experiments in this section and the subsequent modality ablation study (Section 3.7) are conducted on CMAFNet-n, the lightweight variant of the proposed architecture.

The complete CMAFNet achieves the best performance across all metrics, with mAP₅₀ of 0.248, mAP_{50:95} of 0.109, and AP_s of 0.090. These results validate the design rationale of SRM and CSIF: dictionary-based semantic purification enables the network to activate candidate regions for weak-textured and

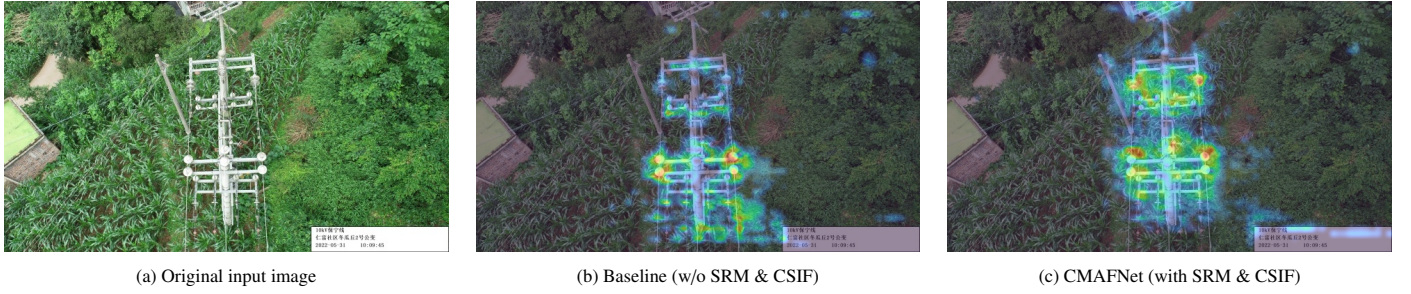


Figure 10: Feature activation heatmaps extracted from the $P_3/8$ -small detection layer. Warmer colors indicate higher activation intensity. The baseline model exhibits diffuse attention spread across background regions, whereas the complete CMAFNet with SRM and CSIF produces spatially concentrated activation patterns that align closely with defect locations, demonstrating that the proposed modules effectively guide the network to focus on genuine targets.

Table 3: Ablation study of CMAFNet under different module configurations. “Wo” denotes removing the corresponding module. The best performance for each metric is highlighted in bold.

Configuration	R	mAP ₅₀	mAP _{50:95}	AP _s	Recall _{jyzwh}	Recall _{dgss}	mAP ₅₀ ^{jyzwh}	mAP ₅₀ ^{dgss}
CMAFNet	0.240	0.248	0.109	0.090	0.450	0.349	0.438	0.396
Wo CSIF	0.222	0.243	0.104	0.087	0.428	0.337	0.418	0.371
Only RGB SRM	0.226	0.235	0.108	0.087	0.437	0.335	0.432	0.378
Only X SRM	0.213	0.226	0.104	0.082	0.425	0.333	0.420	0.367
Wo All SRM	0.224	0.236	0.105	0.086	0.433	0.320	0.426	0.381
Wo All SRM/CSIF	0.217	0.214	0.097	0.074	0.374	0.312	0.359	0.330

geometrically subtle defects that conventional approaches tend to miss, thereby improving recall and small object detection in transmission-line inspection scenarios dominated by small targets.

Removing CSIF causes mAP₅₀ to drop from 0.248 to 0.243 and AP_s from 0.090 to 0.087, while recall decreases from 0.450 to 0.428 for insulator contamination and from 0.349 to 0.337 for conductor strand breakage. These results demonstrate the necessity of CSIF: without global context modeling at the P_5 fusion stage, the network loses the capacity to exploit structural priors—such as the regular arrangement of insulator strings and the spatial relationships between fittings and conductors—for semantic disambiguation of small defects embedded in complex backgrounds.

The single-branch SRM configurations reveal the complementary roles of texture and geometric information. Retaining SRM only on the RGB branch yields mAP₅₀ of 0.235, whereas restricting SRM to the depth branch produces inferior results with mAP₅₀ of 0.226. This asymmetry indicates that RGB imagery remains the dominant information source for small defect discrimination, while depth provides supplementary geometric cues including surface protrusions and boundary discontinuities. When semantic recomposition operates solely on depth features, sensor-specific artifacts—quantization noise, edge bleeding, and missing values at specular surfaces—amplify representational uncertainty, underscoring the necessity of applying SRM to both modalities for statistically aligned feature representations.

Removing all SRM instances while preserving CSIF causes mAP₅₀ to decline to 0.236 and conductor strand breakage recall to drop from 0.349 to 0.320. This demonstrates that global

context modeling alone cannot compensate for the absence of multi-scale semantic purification. The architecture deliberately positions SRM at branch P_3/P_4 levels for intra-modal purification and at fused P_4/P_5 levels for cross-modal enhancement; disrupting this “purify-then-fuse-then-enhance” pipeline forces CSIF to operate on statistically heterogeneous features, limiting the effectiveness of attention mechanisms in establishing meaningful cross-modal correspondences.

The most substantial degradation occurs when both modules are removed, with mAP₅₀ dropping to 0.214 and AP_s to 0.074—representing relative decreases of 13.7% and 17.8%, respectively. Notably, the ablation results reveal a synergistic effect between the two modules: CSIF contributes 2.0% improvement in mAP₅₀ and SRM collectively contributes 4.8%, yet their combined integration yields a total gain of 13.7%, demonstrating non-linear complementary benefits. This synergy arises because SRM addresses cross-modal distribution instability that impedes semantic alignment, while CSIF resolves the limitation of purely local fusion operations lacking long-range structural constraints.

Regarding computational cost, the complete CMAFNet requires only 4.9M parameters and 12.4 GFLOPs. Since removing both modules still requires 5.0M parameters and 11.0 GFLOPs, the proposed modules achieve significant performance improvements with minimal additional overhead.

3.7. Modality Ablation Study

Table 4 reports the modality ablation results. Using RGB images alone significantly outperforms the depth-only setting, indicating that appearance cues remain the dominant source for transmission-line defect detection. However, incorporat-

ing depth information via the proposed CMAF-Net consistently improves all accuracy metrics. In particular, mAP_{50} increases from 0.215 (RGB-only) to 0.243, and AP_s rises from 0.080 to 0.087, demonstrating that depth provides complementary geometric cues, especially for small or low-contrast defects. These results validate both the effectiveness of depth modality and the necessity of cross-modal alignment and fusion.

4. Conclusion

This paper presented CMAFNet, a Cross-Modal Alignment and Fusion Network that addresses the persistent challenges of RGB-D transmission-line defect detection through a principled “purify-then-fuse” paradigm. The proposed architecture systematically tackles three interrelated problems: intra-modal noise contamination arising from illumination artifacts and depth sensor limitations, cross-modal distribution heterogeneity that impedes effective feature alignment, and the absence of global contextual reasoning essential for disambiguating small-scale defects from visually similar background elements.

From a methodological perspective, CMAFNet introduces two complementary mechanisms that collectively enable robust multimodal fusion. The Semantic Recomposition Module performs dictionary-based feature purification by projecting representations into a learned codebook with controllable capacity, creating an information bottleneck that filters modality-specific noise while preserving defect-relevant patterns. The position-wise normalization within SRM transforms cross-modal alignment from implicit weight-based learning into explicit reconstruction-driven enhancement, ensuring that heterogeneous RGB and depth features attain compatible statistical distributions before fusion. The Contextual Semantic Integration Framework subsequently establishes global spatial dependencies through partial-channel attention, enabling the network to leverage structural priors such as the regular arrangement of insulator strings and spatial relationships among transmission components for semantic disambiguation. The partial-channel design, combined with the Adaptive Semantic Regulation Mechanism, prevents the detail erosion and over-smoothing that typically accompany full-channel global attention, thereby preserving the fine-grained discrimination essential for small-object detection.

Extensive experiments on the TL-RGBD dataset, where 94.5% of annotated instances qualify as small objects, demonstrate that CMAFNet achieves substantial improvements over state-of-the-art methods across all evaluation metrics. The full-scale model attains 32.2% mAP_{50} and 12.5% small-object AP, consistently outperforming RGB-based methods across all evaluation metrics. The lightweight configuration achieves 24.8% mAP_{50} at 228 FPS with only 4.9M parameters and 12.4 GFLOPs, outperforming all YOLO variants and matching larger transformer-based detectors at a fraction of their computational cost. Ablation studies further reveal a synergistic relationship between the proposed modules: while SRM and CSIF contribute 4.8% and 2.0% individual gains, their combined integration yields 13.7% total improvement, indicating

non-linear complementary benefits that arise from addressing cross-modal distribution instability and local fusion limitations simultaneously. Modality ablation confirms that depth information provides complementary geometric cues particularly for low-contrast defects and boundary disambiguation that RGB appearance alone cannot capture, validating the necessity of cross-modal fusion for transmission-line inspection scenarios.

Several limitations warrant acknowledgment and suggest directions for future investigation. The current architecture assumes synchronized and spatially aligned RGB-D inputs, which may not hold under all deployment conditions involving diverse sensor configurations or dynamic acquisition platforms. The dictionary-based purification mechanism, while effective for the defect categories present in TL-RGBD, requires empirical tuning of codebook capacity when generalizing to domains with substantially different semantic complexity. Additionally, the performance gap between challenging categories such as insulator contamination exhibiting subtle textural variations and categories with distinctive geometric signatures indicates that adaptive fusion strategies conditioned on defect characteristics may yield further improvements. Future work will explore self-supervised pretraining on unlabeled multimodal inspection data to enhance feature representations, investigate dynamic fusion mechanisms that modulate cross-modal interaction based on input quality, and extend the framework to incorporate temporal consistency constraints for video-based inspection scenarios.

References

Bao, W., Du, X., Wang, N., Yuan, M., Yang, X., 2022. A Defect Detection Method Based on BC-YOLO for Transmission Line Components in UAV Remote Sensing Images. *REMOTE SENSING* 14.

Cao, Y., Xu, H., Su, C., Yang, Q., 2023. Accurate Glass Insulators Defect Detection in Power Transmission Grids Using Aerial Image Augmentation. *IEEE Transactions on Power Delivery* 38, 956–965.

Chen, Y., Han, Y., Huang, W., Shi, J., Li, L., Huang, Z., He, J., Yang, L., 2025. A Novel Identification Model for Potential Electric Hazard Discharge in Transmission Lines Using Multiscale Convolutional Domain Adversarial Network. *IEEE Transactions on Instrumentation and Measurement* 74, 1–14.

Chen, Y., Liu, B., Yuan, L., 2024. PR-Deformable DETR: DETR for Remote Sensing Object Detection. *Ieee Geoscience and Remote Sensing Letters* 21.

Cheng, Y., Liu, D., 2024. AdIn-DETR: Adapting Detection Transformer for End-to-End Real-Time Power Line Insulator Defect Detection. *IEEE Transactions on Instrumentation and Measurement* 73, 1–11.

da Silva, M.F., Honorio, L.M., Marcato, A.L.M., Vidal, V.F., Santos, M.F., 2020. Unmanned aerial vehicle for transmission line inspection using an extended Kalman filter with colored electromagnetic interference. *Isa Transactions* 100, 322–333.

Table 4: Modality ablation of CMAFNet on the TL-RGBD dataset, highlighting the contribution of RGB, depth, and RGB-D fusion inputs to detection capability.

Modality	Params(M)	GFLOPs	P	R	mAP ₅₀	mAP _{50:95}	AP _s	AP _m	FPS	Recall _{jywh}	Recall _{dgss}	mAP ₅₀ ^{jywh}	mAP ₅₀ ^{dgss}
RGB	—	—	—	—	—	—	—	—	—	—	—	—	—
Depth	4.9	12.4	0.497	0.173	0.150	0.060	0.046	0.034	216.6	0.323	0.272	0.265	0.213
RGB+Depth	5.5	12.9	0.452	0.232	0.244	0.103	0.089	0.071	222.3	0.477	0.365	0.431	0.391

Deng, X., He, M., Zheng, J., Qin, L., Liu, K., 2024. Research Progress on Power Visual Detection of Overhead Line Bolt Defects Based on UAV Images. *Drones* 8, 442.

Gupta, S., Girshick, R., Arbeláez, P., Malik, J., 2014. Learning Rich Features from RGB-D Images for Object Detection and Segmentation, in: Fleet, D., Pajdla, T., Schiele, B., Tuytelaars, T. (Eds.), *Computer Vision – ECCV 2014*, Springer International Publishing, Cham. pp. 345–360.

He, M., Qin, L., Wang, Y., Deng, X., Liu, Q., Zhang, Y., Liu, K., 2025. A Weakly Supervised Contrastive Learning Pre-training Method for Visual Defect Detection of Transmission Lines. *IEEE Transactions on Instrumentation and Measurement* 74, 1–15.

Li, C., Shi, Y., Lu, M., Zhou, S., Xie, C., Chen, Y., 2025. A Composite Insulator Overheating Defect Detection System Based on Infrared Image Object Detection. *IEEE Transactions on Power Delivery* 40, 203–214.

Li, Y., Liu, M., Li, Z., Jiang, X., 2023. CSSAdet: Real-Time End-to-End Small Object Detection for Power Transmission Line Inspection. *IEEE Transactions on Power Delivery* 38, 4432–4442.

Liu, X., Miao, X., Jiang, H., Chen, J., 2020. Data analysis in visual power line inspection: An in-depth review of deep learning for component detection and fault diagnosis. *Annual Reviews in Control* 50, 253–277.

Luo, P., Wang, B., Wang, H., Ma, F., Ma, H., Wang, L., 2023. An Ultrasmall Bolt Defect Detection Method for Transmission Line Inspection. *IEEE Transactions on Instrumentation and Measurement* 72, 1–12.

Ma, W., Wang, B., Zhao, Z., Wang, Q., Chen, B., 2025. A Small-Sized Defect Detection Method for Power Line Insulator Using Multiscale Feature and Lightweight Networks in UAV-Vision. *IEEE Transactions on Power Delivery* 40, 2747–2758.

Pouliot, N., Montambault, S., 2012. Field-oriented developments for LineScout Technology and its deployment on large water crossing transmission lines. *Journal of Field Robotics* 29, 25–46.

Shen, F., Cui, J., Li, W., Zhou, S., 2025. TinyDef-DETR: A Transformer-Based Framework for Defect Detection in Transmission Lines from UAV Imagery. *Remote Sensing* 17, 3789.

Song, Y., Wang, H., Zhang, J., 2014. A Vision-Based Broken Strand Detection Method for a Power-Line Maintenance Robot. *IEEE Transactions on Power Delivery* 29, 2154–2161.

Tan, M., Pang, R., Le, Q.V., 2020. EfficientDet: Scalable and Efficient Object Detection, in: 2020 IEEE/CVF Conference on Computer Vision and Pattern Recognition (CVPR), IEEE, Seattle, WA, USA. pp. 10778–10787.

Wang, H., Yang, Q., Zhang, B., Gao, D., 2024. Deep learning based insulator fault detection algorithm for power transmission lines. *Journal of Real-Time Image Processing* 21, 115.

Wang, Y., Qu, Z., Hu, Z., Yang, C., Huang, X., Zhao, Z., Zhai, Y., 2025. Cross-Domain Multilevel Feature Adaptive Alignment R-CNN for Insulator Defect Detection in Transmission Lines. *IEEE Transactions on Instrumentation and Measurement* 74, 1–12.

Wu, D., Yang, W., Li, J., Du, K., Li, L., Yang, Z., 2025. CRL-YOLO: A Comprehensive Recalibration and Lightweight Detection Model for AAV Power Line Inspections. *IEEE Transactions on Instrumentation and Measurement* 74, 1–21.

Xu, C., Li, Q., Zhou, Q., Zhang, S., Yu, D., Ma, Y., 2022a. Power Line-Guided Automatic Electric Transmission Line Inspection System. *IEEE Transactions on Instrumentation and Measurement* 71, 1–18.

Xu, C., Li, Q., Zhou, Q., Zhang, S., Yu, D., Ma, Y., 2022b. Power Line-Guided Automatic Electric Transmission Line Inspection System. *IEEE Transactions on Instrumentation and Measurement* 71, 1–18.

Yang, L., Kong, S., Deng, J., Li, H., Liu, Y., 2023. DRA-Net: A Dual-Branch Residual Attention Network for Pixelwise Power Line Detection. *IEEE Transactions on Instrumentation and Measurement* 72, 1–13.

Yi, J., Liu, T., Mao, J., Wang, Y., Zhang, H., Xie, H., Zhong, H., Chang, X., 2025. Toward Efficient Power Scene Detection via Topology-Preserved Knowledge Distillation. *Ieee Transactions on Industrial Informatics* 21, 8812–8823.

Zhang, K., Zhou, R., Wang, J., Xiao, Y., Guo, X., Shi, C., 2024a. Transmission Line Component Defect Detection Based on UAV Patrol Images: A Self-Supervised HC-ViT Method. *IEEE Transactions on Systems, Man, and Cybernetics: Systems* 54, 6510–6521.

Zhang, W., Li, X., Wang, L., Zhang, D., Lu, P., Wang, L., Cheng, C., 2025a. A Lightweight Method for Road Defect Detection in UAV Remote Sensing Images with Complex Backgrounds and Cross-Scale Fusion. *Remote Sensing* 17, 2248.

Zhang, X., Zhang, Y., Shen, K., Fu, Q., Shen, H., 2025b. FAFNet: An Overhead Transmission Line Component Detection Method Based on Feature Alignment and Fusion. *IEEE Sensors Journal* 25, 30197–30206.

Zhang, Y., Li, B., Shang, J., Huang, X., Zhai, P., Geng, C., 2024b. DSA-Net: An Attention-Guided Network for Real-Time Defect Detection of Transmission Line Dampers Applied to UAV Inspections. *IEEE Transactions on Instrumentation and Measurement* 73, 1–22.

Zhao, F., Zhang, C., Geng, B., 2024. Deep Multimodal Data Fusion. *ACM Computing Surveys* 56, 1–36.